J Mater Sci: Mater Electron (2015) 26:1709–1718
DOI 10.1007/s10854-014-2597-4

Structure and magnetic properties of $Ni_{0.64}Zn_{0.36}Fe_2O_4$ nanoparticles synthesized by high-energy milling and subsequent heat treatment

Abdollah Hajalilou · Mansor Hashim · Halimah Mohamed Kamari

Received: 19 October 2014 / Accepted: 6 December 2014 / Published online: 12 December 2014

Abstract High energy ball milling and subsequent annealing were applied to synthesize nanocrystalline $Ni_{0.64}Zn_{0.36}Fe_2O_4$ ferrite from a powder mixture of pure metal Zn, Fe_2O_3 and NiO in an oxygen atmosphere. The structural and phase evolution of powder particles after different milling times were studied by X-ray diffractometry. The XRD results showed that a Ni–Zn ferrite was formed with some residual Fe_2O_3 by annealing a 30-h-milled sample at as low as 400 °C for 2 h. The average crystallite size of the 30 h-milled powder was estimated to be about 15 nm which grew to 21 nm after annealing at 500 °C for 2 h. TEM image showed an agglomerated state of particles for 30 h-milled powders. FT-IR analysis indicated two absorption bands in the Ni–Zn ferrite structure related to octahedral and tetrahedral sites, respectively, in the range of 400–600 cm^{-1}. Thermogravimetric analysis showed a mass loss about 2 % for as-received powder mixture below 400 °C; after that, it was almost stable. The Ni–Zn ferrite formation mechanism was detected to be in three stages: oxidation of zinc, diffusion of ZnO in Fe_2O_3 and the formation of $ZnFe_2O_4$, and diffusion of NiO in $ZnFe_2O_4$ and the formation of Ni–Zn ferrite. Vibrating sample magnetometery results revealed that a saturation magnetization of the 30 h-milled sample was about 5 emu/g which increased to 16 emu/g after annealing at 400 °C due to a reduction in density of lattice imperfections and strain.

A. Hajalilou (✉) · M. Hashim
Materials Synthesis and Characterization Laboratory, Institute of Advanced Technology (ITMA), Universiti Putra Malaysia (UPM), 43400 Serdang, Selangor, Malaysia
e-mail: e.hajalilou@yahoo.com

H. Mohamed Kamari
Physics Department, Universiti Putra Malaysia (UPM), 43400 Serdang, Selangor, Malaysia

1 Introduction

In the past few decades, there has been much focus on the several novel and non-equilibrium processing techniques to improve and develop the performance of the existing advanced ferrite materials by synthesizing nano-sized crystalline structure [1]. These involve high energy ball milling, vapor deposition, rapid solidification from the liquid state and plasma processing. Indeed, the unique chemical, physical and magnetic properties of nanocrystalline materials compared to a bulk and coarse-grained polycrystalline materials are drawn from the large number of atoms which exist in a lattice defect domain such as grain boundaries, interface and dislocations [1, 2]. Thus, the microstructure especially crystallite size is the most important factor in determining the magnetic properties such as a hysteresis loop of soft magnetic ferrites [2].

The high energy ball milling route which encompasses a chemical reaction during milling is often considered as a mechanosynthesis or mechanochemical synthesis [3–5]. It is possible to synthesize advanced materials and obtain a very fine microstructure by this method. This is due to the frequent fracturing and cold re-welding of powder particles, transferring of materials by diffusion of components, creating of severe plastic deformation, generating a wide variety of lattice defects during the milling process [3]. Moreover, the mass transformed produced during the milling process enables commercial compounds to be produced at room temperature, enhancing their properties, especially soft magnetic materials by subsequent heat treatment [6].

Soft magnetic materials generally fall into two categories: (1) ceramic materials (mainly ferrites) and (2) metallic alloys (mainly Fe-based alloys). The Ni–Zn ferrites have a normal spinel structure with a general chemical formula of AB_2O_4 in which Fe^{+3}/Zn^{2+} and Fe^{+3}/Ni^{2+} cations reside in tetrahedral (A) sites and an octahedral (B) sites, respectively [7]. These soft magnetic materials have versatile technological applications due to the involvement of remarkable magnetic properties such as high electrical resistivity, high permeability, and low power loss in high frequency [8, 9]. Additionally, a low saturation magnetization and high coercivity were observed in nano-sized structure of ferrites [10]. It is widely used in radio frequency circuits, rod antennas, high quality filters and read/write heads for high speed digital tapes [7, 11].

The nano-sized spinel-phase Ni–Zn ferrites are usually synthesized by the sol–gel method [12], combustion method [13], thermohedral synthesis [14], conventional solid-state reaction [15], and mechanochemical process [16]. Sometimes, a crystal aggregation of all sorts occurs after thermal deposition and drying in wet-chemistry synthesis techniques. Moreover, in a solid-state route a high temperature is required for crystallization. Thus, to reduce the problematic issues, the mechanochemical reaction route was used in this study to synthesize ferromagnetic $NiZnFe_2O_4$ nano powder particles and subsequent heat treatment was applied to improve magnetic properties. Additionally, the formation mechanism of the $NiZnFe_2O_4$ single phase in the oxygen atmosphere is discussed.

2 Experimental

An oxygen environment was selected for mechanical activation of a powder mixture of Zn, NiO and Fe_2O_3 to synthesize a $Ni_{0.64}Zn_{0.36}Fe_2O_4$ ferrite nanopowder. For this purpose, the starting materials without further purification Zn (99.5 % purity), NiO (99.7 % purity) and Fe_2O_3 (99.5 % purity), purchased from Alpha Aesar, were mixed based on molar ratio and applying the following reaction:

$$0.64\ NiO + 0.36\ Zn + Fe_2O_3 = Ni_{0.64}Zn_{0.36}Fe_2O_4 \qquad (1)$$

In order to have a sufficient amount of powder for executing of different experimental analysis, a ball to powder ratio was chosen to be 10:1. Subsequently, 2.98 g of NiO powder and 1.47 g of Zn were mixed with 9.98 g of Fe_2O_3 so that a total powder mass was 14.43 g.

Then, ball milling of powder mixture was executed in a planetary ball mill at room temperature and under oxygen atmosphere. The ball milling media were hardened chromium steel vial (150 ml) with five hardened steel balls (18 mm). Finally, the rotational speeds of the vial and the disc were fixed at 600 and 400 rpm, respectively, and the powders were activated for different periods ranging from 0 to 30 h. It is worth mentioning that the milling machine is adjusted in such a way to have a 15 min rest after every 1 h milling. This was to prevent the powder agglomeration. After the ball milling process, 30 h-milled samples were selected to anneal at different temperatures for 2 h.

Phase and structural evaluation were carried out applying an X-ray diffraction (XRD) at a diffraction angular range of $2\theta = 20°–80°$ and using Cu Kα [wave length (λ) = 0.154 nm].

Field emission scanning electron microscopy (FeSEM) using a JEOL JSM-7600F machine equipped with energy-dispersive X-ray spectroscopy (EDX) was employed to evaluate a powder particles morphology and microstructure. Transmission electron microscopy (TEM) analysis of the samples was carried out by using a 75 kV Hitachi 7100 TEM (Tokyo Japan).

The Fourier transform Infrared (FT-IR) transmission spectral data of the activated samples mixed with the reference KBr powder were taken from 4,000 to 350 cm^{-1} using the Jasco-680-plus (Tokyo, Japan) spectrophotometer.

The vibrating sample magnetometer (VSM) was used to study the magnetic properties of the samples at room temperature.

The differential thermal analysis (DTA), thermogravimetric analysis (TGA) (TGA/SDTA 51E/LR1600/MT5/347) and differential scanning calorimetry (DSC) were used to study the thermal characteristics of the samples. The experiments for thermal analysis were carried out in an ambient air atmosphere in the range of 0–1,000 °C. The heating rate was chosen to be constant at 10 °C/min.

3 Results and discussions

3.1 Thermal analysis

Thermal characteristics of as-received powder were analyzed by a differential thermal analysis (DTA) and a simultaneous thermal analyzing (TG-DSC) machine in ambient air atmosphere. Figure 1 displays the DTA traces accompanied by TG and DSC curves of the as-received Zn, NiO and Fe_2O_3 powder mixture. The DSC traces revealed the emergence of an endothermic peak around 417 °C, which can be associated with zinc local melting. This is speculated from thermodynamic data in which all reactions in the system of Zn/NiO/Fe_2O_3 are exothermic except for the local melting of zinc. Furthermore, an existence a small hump around 600 °C can be attributed to $ZnFe_2O_4$ solid-solution formation. Continually rising baseline also suggests the solid-state diffusion reaction mechanism of the Ni–Zn ferrite formation.

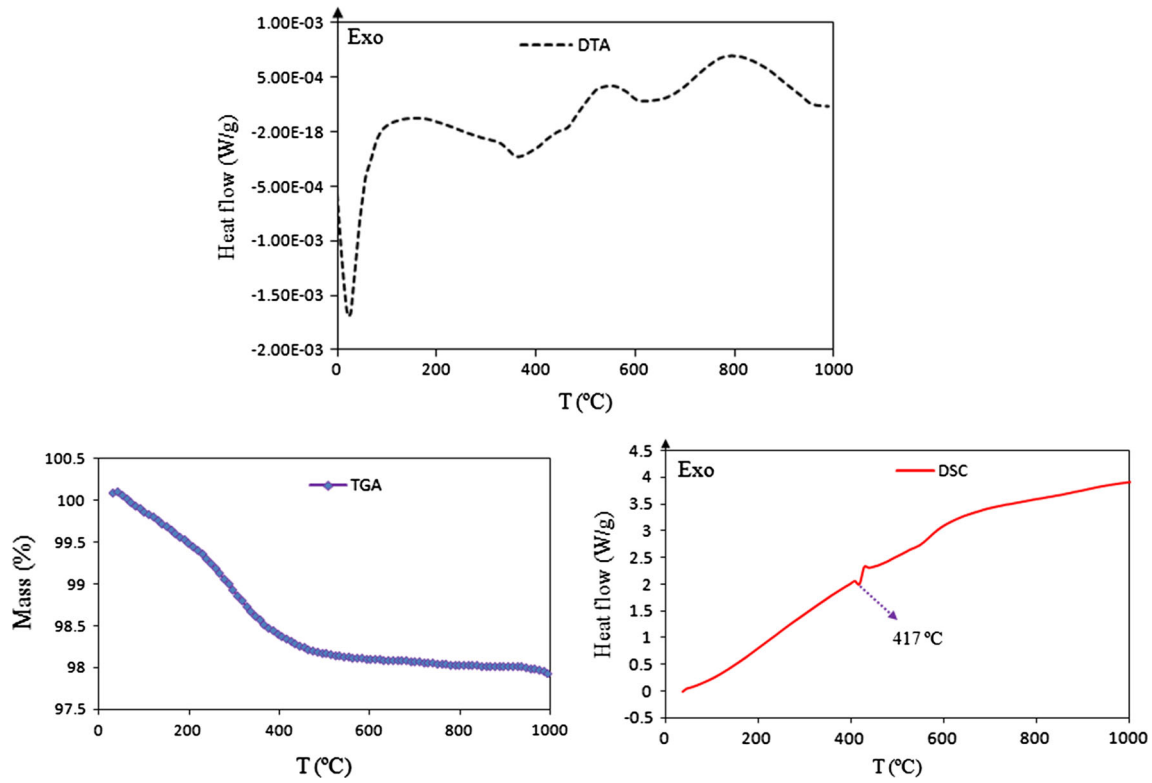

Fig. 1 DSC, TG and DTA traces of as-received Zn/NiO/Fe_2O_3 powder mixture

The DTA traces indicated the maximum of the first large endothermic peak at around 50 °C. This peak looks like corresponding to a release of some gaseous species from the samples. Another endothermic peak around 400 °C was followed by two big exothermic peaks around 580 and 800 °C. The endothermic peak may be related to the local melting of zinc. Among the two exothermic peaks, the first one can be concerned with $ZnFe_2O_4$ solid-solution formation and the second one can be attributed to the Ni-Zn ferrite formation. The TG traces had an L-like shape characteristic suggesting that a mass change took place during heating in a calorimeter. A mass loss was observed about 2 % below 400 °C. This can be associated with evaporation of the absorbed water from the sample so that after 400 °C it became stable.

3.2 Structural evaluation

The X-ray diffraction patterns of Zn, NiO and Fe_2O_3 powders are involved: after only a simple mixing and without activation operation; also after different milling times and subsequent heat treatment of those 30 h-milled samples the XRD results are exhibited in Fig. 2. According to the International Centre for Diffraction Data (ICDD), the intense peaks of Zn (ICDD PDF#01-087-0713), Fe_2O_3 (ICDD PDF#01-1053) and NiO (ICDD PDF#04-0833) are evident in the XRD pattern of starting mixture of powders. According to the ICDD file, the three major peaks of Zn with high intensity are located in the Bragg's diffraction angels (2θ) of 43.221 (I = 100), 36.290 (I = 39.6), 39.04 (I = 23.3) with which the peak for $2\theta = 43.221$ is compliant with an NiO peak. After the milling process, after 2 h, the Zn peaks completely vanished. It seems to happen in one of the two conditions: (1) Zn becoming amorphous, (2) Zn diffusing into the Fe_2O_3 lattice structure.

Regarding the thermodynamic information (as written below), the oxidation of zinc in the oxygen environment is so exothermic reaction in such a way that by providing a small amount of activation energy it can be promoted by a combustion mode.

$$Zn(s) + 1/2O_{2(g)} = ZnO_{(s)},\ \Delta G^{\circ}_{298} = -308.3\ \text{kJ/mol} \tag{2}$$

$$\frac{(\Delta H_f^{\circ})_{ZnO}}{(C_p)_{ZnO}} = \frac{348\,\text{kJ/mol}}{40.25 \times 10^{-3}\,\text{kJ/mol}} \approx 8.65 \times 10^3\,\text{k} > 2.0 \times 10^3\,\text{k} \tag{3}$$

where ΔH°_f is the enthalpy of ZnO formation and C_p is the heat capacity at the standard state [17]. As stated in previous studies [17], it has been practically indicated that, once ignited, the reaction will be completed in a self-propagating combustion mode when the action with a ratio—$\Delta H^{\circ}_f/Cp$ of $>2 \times 10^3$ K.

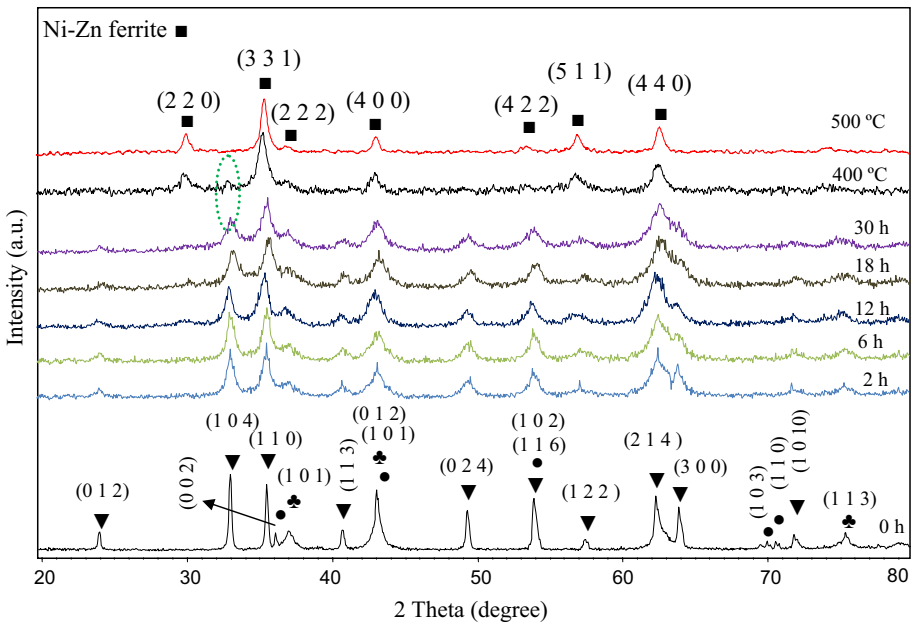

Fig. 2 XRD patterns taken from the Zn/NiO/Fe_2O_3 powder mixture; after different milling times and annealing a 30 h-ball milled at 400, 500 °C; Fe_2O_3 (*Black down pointing triangle*), NiO (*Black club suit*), Zn (*Filled circle*)

It suggested that within 6 h milling essentially a $ZnFe_2O_4$ solid solution has been produced from the Fe_2O_3 and ZnO phases. The results are consistent as attained by Bid and Pradhan [7] which indicated the formation of $ZnFe_2O_4$ could take place within only 30 min of ball milling with homogeneous stoichiometric (1:1 mol%) powder mixture of Fe_2O_3 and ZnO phases.

It is worthy to mention that the content of each phase (%) was computed from the integrated XRD peak intensities based on the equation below:

$$W_X = \frac{A_x^{(hkl)}}{\sum x A_x^{(hkl)}} \quad (4)$$

where W_X is the evaluated fraction for one compound and $Ax^{(h\ k\ l)}$ its integrated diffraction intensity of the major peak of compound X. The content (wt%) of Fe_2O_3 was raised at the beginning and then reduced during milling. After 12 h of milling, the content of Fe_2O_3 decreased quickly (about 36.2 %) while the content of NiO decreased very slowly (about 10.31 %). Due to the large crystallite size (less reactive) of NiO at 12 h milling, it led to just a small amount of diffusion of NiO into the ZnF_2O_4 lattice structure. By extending the milling time until 18 h, the contents (wt%) of both NiO and Fe_2O_3 phases approximately decreased constantly. Eventually, at 30 h milling time, the contents (wt%) of NiO and Fe_2O_3 reduced to 6.802 and 16.21, respectively. Additionally, the XRD diffraction peaks of phases showed that by increasing the milling time the position of the Braggs diffraction angles shifted to lower degrees in such a way that this shifting until 18 h was significant but after that it was trivial. This can be accounted for by their atomic radius for which the zinc atomic radius is closer to that of Ni rather than that of Fe. The diffusion rate of NiO in Fe_2O_3 phase is much slower than the diffusion of ZnO in Fe_2O_3 phase. The reason is due to the fact that, as it has been stated in previous studies [7], in spinel ferrite the Ni^{2+} ions would favor to locate in the octahedral sites while these places have already taken up by Fe^{3+} ions, thus, it leads to a very slow rate of diffusion of Ni^{2+} ions. Penetration/diffusion of Zn^{2+} with an ionic radius of 0.84 Å into the Fe_2O_3 structure led to the generation of $ZnFe_2O_4$ solid solution. The formation of this compound is thermodynamically favorable at room temperature because it involves a negative value of ΔG°_{298}. The negative ΔH°_{298} also suggests that this reaction is exothermic.

$$\Delta H^{\circ}_{298} = -12.4569\ \text{kJ/mol} \quad (5)$$

$$\Delta G^{\circ}_{298} = -9.2396\ \text{kJ/mol} \quad (6)$$

Moreover, the formation of $ZnFe_2O_4$ during milling also can be associated with the spin arrangement in such a way that the spins either have the onset of intersublattice exchange interaction of Fe^{3+}(A)–O^{2-}–Fe^{+3}[B] type occurring because of the mechanically induced inversion and/or have the onset of intrasublattice exchange interaction type with deformed bond angles [18].

From the point of view of crystal structure, simultaneously occurring events mentioned just above caused the width of phase peaks to be broadened and their intensity slightly decreased during the milling process. The ball milling route is often concerned with the reduction of the intensity and broadening of the crystalline diffraction peaks. This is due to the decreasing crystallite size to the nano scale as well as an increasing internal lattice strain.

The induced modifications in the size of crystallite and lattice strain of NiO and Fe_2O_3 phases during the ball milling process were evaluated by the X-ray diffraction peak broadening and approaching of Williamson-Hall equation [19] as well as X'Pert HighScore software and their results tabulated in Table 1.

$$b\cos\theta = \frac{K\lambda}{d} + 2A\sqrt{\varepsilon^2}\sin\theta \quad (7)$$

where d, η, λ, b, θ. are referring to the average crystallite size (nm), internal lattice strain (%), wavelength (0.145 nm), the diffraction peak width at half-maximum intensity and Bragg's diffraction angle (rad). A is a coefficient which relies on the strain distribution and K is the Scherrer constant (usually taken to be 0.91). It is worth mentioning that the details of crystallite size and lattice strain calculation have been reported in our previous published paper [20].

The Fe_2O_3 phase particle sizes immediately decreased at the beginning of the milling operation and remarkably reduced from 85 to 13 nm just within 6 h milling. Then, they declined very slowly up to 12 h so that by extending the milling time to 30 h, a saturation value of 5 nm was obtained. About the NiO particle size, it reduced from 27 to 9 nm within the 6 h milling operation. Afterward, the particle size became smaller very slowly by incrsing the milling time to 12 h. By extending the milling until 18 h approximately, no further reduction in the particle size was detected. After that the constant rate declined and finally fell down to almost the same size as Fe_2O_3 phase particle size. Contrarily, the lattice strain of both phases increased by increasing milling time approximately in the same manner. However, the obtained values of $<\varepsilon>^{1/2} \times 10^3$ (r.m.s strain) were 9.8 and 7.1 %, respectively, for NiO and Fe_2O_3 phases after 30 h milling.

During the milling process, due to the collision of powder/ball/vial, they deform, fracture and reweld, resulting in the refinement of crystallite size as well as a generation and increasing a huge number of lattice defect densities such as grain boundaries and dislocations. This, in turn, causes variation in the lattice strain of powder particles. The creation of this kind of defects and refinement of crystallite size during the milling process results in providing short-circuit diffusion routes which it can promote the reaction kinetics and also lead to a decreasing of the synthesis temperature of materials [3]. As can be observed from the table, by elevating the milling time both the lattice constants of the Fe_2O_3 rhombohedral phase, namely "a" and "c", vary an anisitropically and nonlinearly. The value of "a" enhanced slowly at the initial step of milling (2 h MA) and quickly up to 6 h of milling and afterward remained approximately constant until the 30 h milling. Whereas the "c" changed in the same manner but a downward trend. The enhanced value of "a" even under compressive stress of ball-powder/ball-vial collision can be associated with the substitution of Fe^{+3} ions (Oct. radius = 0.65 Å) by larger Ni^{+2} ions (Oct. radius = 0.69 Å) along a-axis. Likewise, the substitution of Fe^{+3} ions by smaller Zn^{+2} ions (Oct. radius 0.60 Å) along c-axis led to the contraction of c-axis. The lattice parameter of NiO phase approximately increased continually by increasing milling time due to the induced lattice defects during the milling process.

By annealing a 30-h activated sample at lower temperature of 400 °C, however, a Ni–Zn ferrite was formed. The existence of Fe_2O_3 phase peak at $2\theta \sim 33°$ indicted that the reaction was not completed yet. The diffraction peaks corresponding to the NiO/ZnO/Fe_2O_3 were not found in the diffraction patterns. By increasing the annealing temperature to 500 °C, the XRD pattern suggests that the reaction between those of the precursor oxide was completed and single phase $Ni_{0.64}Zn_{0.36}Fe_2O_4$ was formed. By analyzing the ferrite diffraction peaks intensity produced and a comparison with reference JCPDS file (ICDD PDF#98-006-8765) detected, the peaks did not obey the reference. This mismatching indicates that the $Ni_{0.64}Zn_{0.36}Fe_2O_4$ phase had a disordered cation distribution and inhomogeous structure compared to the ordered structure. By

Table 1 The variation of average crysatllite size and lattice strain as well as lattice parameter of the NiO, and Fe_2O_3 powder particles as a function of milling time

Milling time (h)	Fe_2O_3				NiO		
	Crystallite size (nm)	Lattice parameter (nm)		r.m.s. strain × 10^3, $<\varepsilon^2>^{1/2}$	Crystallite size (nm)	Lattice parameter (nm)	r.m.s. strain × 10^3, $<\varepsilon^2>^{1/2}$
		a	c				
0	85	0.5034	1.3752	0.7945	27	0.4179	0.1518
2	13	0.5037	1.3728	2.908	16	0.4180	6.320
6	10	0.5041	1.3724	5.268	10	0.4181	6.848
12	9	0.5045	1.3686	6.289	9	0.4187	7.632
18	7	0.5088	1.3567	6.786	8	0.4192	8.231
30	5	0.5122	1.3587	7.241	5	0.4198	9.156

increasing the annealing temperature to 500 °C, no new phases were observed, indicating that the Ni–Zn ferrite produced is stable at high temperatures. The diffraction peak intensy of $Ni_{0.64}Zn_{0.36}Fe_2O_4$ ferrite increased and their width decreased. In fact, during the annealing process the internal stress induced in the milling is being diminished and the lattice relaxation occurring, thereby resulting in re-ordering of the metallic ions between octahedral and tetrahedral sites [7]. The average crystallite size of the 30 h-milled powder was estimated to be about 15 nm which grew to 21 nm after annealing at 500 °C for 2 h. On the other hand, the lattice strain decreased from 0.701 % (30 h-milled) to 0.573 % after annealing at 500 °C.

3.3 Morphological changes evaluation

Figure 3 displays a FeSEM and TEM images of 30 h milled sample accompanied by its EDX spectra and its particle size distribution histogram. The FeSEM images indicated that the powder particle was stuck to each other and agglomerated after the 30 h milling which was confirmed by the TEM image. This suggests that for a higher milling time cold welding overcomes the fracturing. In fact, by increasing the milling time the powder particles become smaller and heat released from the reactants caused a temperature increase inside the vial. Eventually, the long duration of 30 h milling led to the agglomeration of powder particles. The EDX spectrum clearly reveals the Fe, O, Zn and Ni peaks, indicating that the operation of the milling process has not introduced any impurity into the milled powders. C peaks detected in the spectrum were because of the carbon tape used on the Al stub.

A broad distribution of particle sizes in the 30 h-milled sample was observed; with distribution in the range of 8–65 nm and with average particle size of 28 nm. This is due to the fact that high amounts of stress induced during the milling process caused an agglomeration of powder particles.

TEM micrographs of the 30 h-milled samples sintered at 400 and 500 °C are shown in Fig. 4. The TEM images indicate that the particle sizes grew as compared to the 30 h-milled samples but they were not remarkable. An

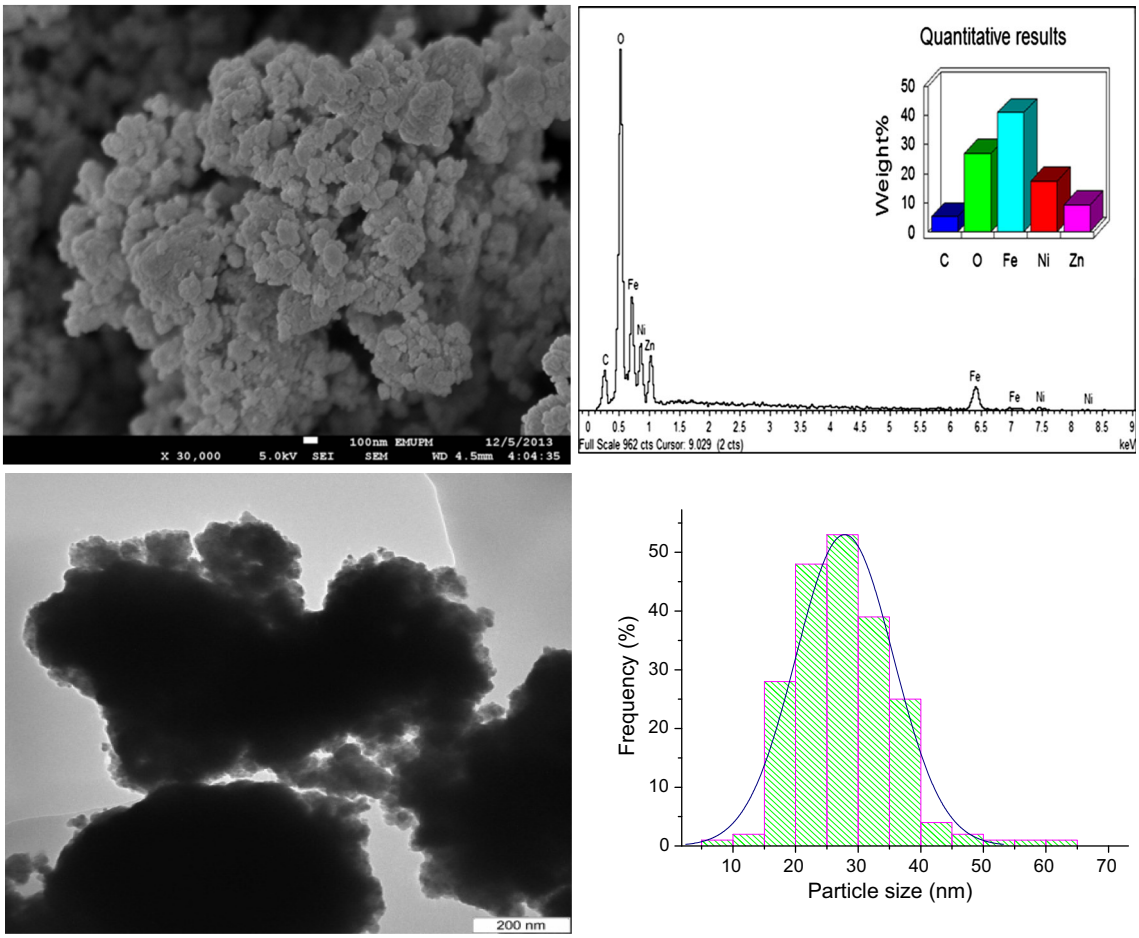

Fig. 3 FeSEM, TEM images and EDX spectra of 30 h-milled sample

observation the agglomerated particles may either be associated with the induced stress during the milling process or magnetic behavior of particles.

3.4 Absorption band evaluation by FT-IR spectroscopy

To further study $Ni_{0.64}Zn_{0.36}Fe_2O_4$ ferrite single phase characteristics and chemical bands, the FT-IR spectroscopy was carried out. The absorption bands of solids at 100–1,000 cm^{-1} are often associated with the ions vibration in the crystal lattice [21–23]. The absorption bands of oxide often are situated in the range of 400–1,100 cm^{-1}. The stretching vibration bands of Zn–O, Ni–O and Fe–O are detected to be in the range of 450–700, 400–500 and 900–1,000 cm^{-1}, respectively [21–23]. Waldron identified the continuously bonded crystals in the ferrite structure [21] and they involve two sublattices of octahedral (O) and tetrahedral (T), the O-band and T-band are attributed to the intrinsic vibration of $Ni^{2+}$and Zn^{2+} ions. Figure 5a, b show the room temperature FT-IR spectra for ball milled samples after different milling times and 30 h-milled samples after being annealed at 500 °C in the range of 350–4,000 cm^{-1}. As can be observed, three main absorption bands appeared on FT-IR spectra in the ball-milled samples. According to the mentioned references above, they are associated with Ni–O, Zn–O and Fe–O bands in the initial powder mixture, respectively. By looking closely, the Fe–O bands shifted from 1,050 to 950 cm^{-1} after 6 h milling. This variation certainly suggests some occurrences. This, already by XRD, determined that the formation of $ZnFe_2O_4$ solid solution occurred during this period of time. The other noticeable variation was observed between 12 and 18 h millings, in such a way that the Fe–O bands moved to higher wavelength and the Zn–O and Ni–O bands approximately vanished. This suggests that by increasing the milling time the NiO phase was diffused into the $ZnFe_2O_4$ phase structure. After annealing the 30 h-milled samples at 500 °C, the Fe–O absorption was removed and two absorption bands were observed around 471 cm^{-1} which is assigned as O (octahedral) band and another at around 576 cm^{-1} which is assigned as T (tetrahedral). This shows that Fe ions are distributed between octahedral and tetrahedral sites as well as formation of $Ni_{0.64}Zn_{0.36}Fe_2O_4$ single phase. Moreover, the small induced spectrum at around 1,650 cm^{-1} is related to the absorbed water and at around 1,400 cm^{-1} hydrocarbon impurity of powders.

3.5 Magnetic behavior evaluation

The magnetization trait of the ferrite is typical of soft ferro- and ferrimagnetic order which can be described on the basis of changes in the exchange interaction between octahedral and tetrahedral sub-lattices. However, there is an interaction of four aspects namely the spin canted effect, magneto-crystalline anisotropy, super-exchange interaction, and dipolar interactions between the moments present on the surface of nanoparticles of ferrites. Thus, the magnetic behavior depicted in nano particles of a soft magnetic ferrite is an intextricable effect of these interactions [24–26].

Room temperature M–H hysteresis loops of the 30 h-milled as well as the 30 h-milled annealed sample at 400 °C are shown in Fig. 6. The hysteresis curve for the 30 h-milled sample, with average particle size of 28 nm, is 'S'-shaped with low coercivity, Hc = 140 Oe, which is characteristic of superparamagnetism [27, 28]. Once the crystal lattice extends only over a few nanometers, the surface atoms become crucial and may lead to a net magnetization [27]. Hence, for nanostructured Ni–Zn ferrite samples, it was expected magnetic properties would have a strong dependence on the average particle size. The value of the saturation magnetization (Ms) and uncompensated magnetic moment (μ) of the samples were estimated using the Langevin Equation as follows;

$$M\ (H)\ =\ Ms\ [\coth\left(\frac{\mu H}{k_B T}\right)-\frac{k_B T}{\mu H} \tag{8}$$

where k_B is the Boltzmann's constant and T is the absolute temperature and M (H) is the magnetization for an applied filed H [27]. The values of Ms and μ for the 30 h-milled sample were found to be 5.2 emu/g and 0.662 μ_B, where μ_B is the Bohr magneton, respectively.

The rather low value of Ms for the 30 h-milled sample is due to the existence of the remaining initial oxides, the very small crystallite size and high density of structural defects and internal lattice strain.

Annealing the 30 h-milled sample at 400 °C led to the increment of Ms to 16 emu/g. This is because of the increase in the degree of crystallinity in the annealed sample. From the XRD patterns, for example for 2θ at 35°, the XRD peak intensity for the annealed sample was 4,082.65 (counts) which is 41 % larger than the peak intensity of the 30 h-milled sample, 1,683.32 (counts). Another reason for increase Ms of the annealed sample can be attributed to the relaxation of the induced canted spin arrangement and non-equilibrium cation distribution from the ball milling towards the equilibrium configuration. Furthermore, a relationship between Ms and annealing temperature can be expressed as follows;

$$Ms = 8.166\ \exp\left(\frac{3T}{1000}\right) \tag{9}$$

where T is temperature. The increase of Ms with the annealing temperature may be attributed to the solid-state diffusion of the remaining content of initial oxides into the Ni–Zn ferrite spinel structure as well as the elimination of internal lattice strain and reduction of the grain boundary

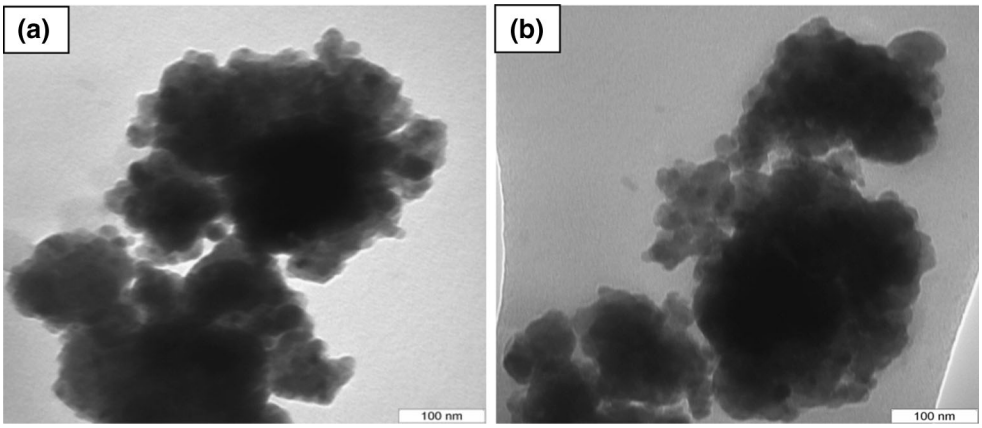

Fig. 4 TEM images of 30 h-milled sample annealed at **a** 400 °C and **b** 500 °C

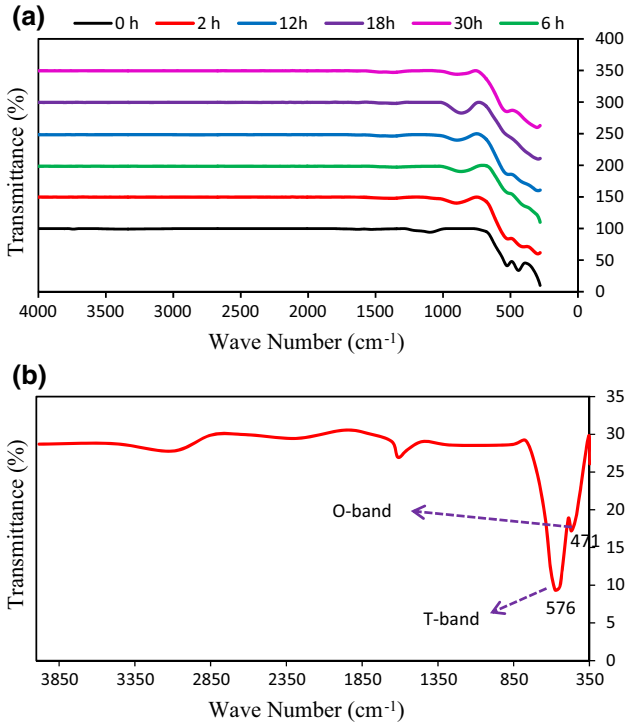

Fig. 5 Infrared spectra in the 4,000–350 cm^{-1} range for nanocrystalline $Ni_{0.64}Zn_{0.36}Fe_2O_4$; **a** after different milling times and **b** 30 h-milled samples annealed at 500 °C

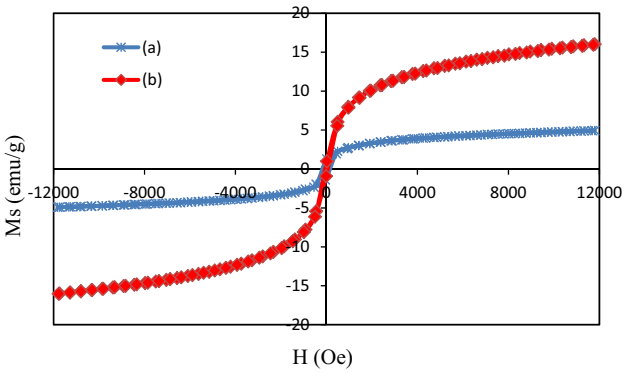

Fig. 6 Room temperature hysteresis loop of Ni–Zn ferrite for (*a*) 30 h-ball milled, (*b*) 30 h-ball milled annealed at 400 °C

volume fraction. Since the particle growth at 400 °C sintering was not significant, the surface of the particle or the grain boundary plays key role in the Ni–Zn ferrite magnetic behaviors. In fact, the ground-state magnetic arrangement of atoms located in the interfacial of at the surface is different from that seen in the corresponding bulk one [29]. In this study, the Ms value (16 emu/g) is also considerably smaller (∼41 %) than the Ms for bulk Ni–Zn ferrite (67 emu/g) [30]. The reason can be associated with the spin canting that dominates over the effect of the cation site exchange in the surface induced from the ball milling of the powder [31]. In fact, transition metal ions in the spinel lattice interact with oxygen atoms and results in reduction of the net magnetic moment in the particles. This effect is especially noticeable for ultrafine particles with nanometer size because if involves a large surface to volume ratio [32].

On the other hand, a decreasing value of coercivity (Hc) from 140 Oe (30 h-milled sample) to 102 Oe (30 h-milled sample which was annealed at 400 °C can be attributed to the defect elimination and residual stress relaxation. For example, the lattice strain of 0.701 % for 30 h-milled sample reduced to 0.611 % after subsequent annealing at 400 °C for 2 h. It is evident that the value of Hc did not follow the Herzer's random anisotropy model (Hc $\propto D^6$; where D is the average particle size). This may arise from the high level of structural defects and residual stress induced from the ball milling process.

4 Conclusion

Ball milling a mixture of $Zn/Fe_2O_3/NiO$ powder in the oxygen atmosphere until a 30 h-mechanical activation could not provide a sufficient energy to produce a

$Ni_{0.64}Zn_{0.36}Fe_2O_4$ ferrite. By annealing 30 h-activated powders at a temperature as low as 500 °C for 2 h a single phase of $Ni_{0.64}Zn_{0.36}Fe_2O_4$ ferrite with crystallite size of 21 nm was produced. FT-IR spectra indicated an existence of metal oxide bands (T-band and O-band) in the ferrite structure obtained. The phase transformation kinetics was detected by the initial formation of zinc ferrite. Then, NiO diffused into the $ZnFe_2O_4$ ferrite lattice structure to form a single phase of $Ni_{0.64}Zn_{0.36}Fe_2O_4$ ferrite. The VSM analysis revealed that $Ni_{0.64}Zn_{0.36}Fe_2O_4$ nanopowders had a superparamagnetic behavior which is possible to achieve in ultrafine structures since a very fine size of the $Ni_{0.64}Zn_{0.36}Fe_2O_4$ ferrite particle was confirmed by TEM analysis. The annealing process led to the increase of saturation magnetization and reduction of coercivity of the samples. The occurrence of these phenomena can be associated with the elimination of internal stresses induced during the milling, reduction density of lattice defects as well as re-arrangement of cations in the $Ni_{0.64}Zn_{0.36}Fe_2O_4$ spinel phase structure.

Acknowledgments The corresponding author would like to appreciate University Putra Malaysia Graduate Research Fellowship section for providing financial support for this work.

References

1. M. Stefanescu, M. Stoia, C. Caizer, O. Stefanescu, Preparation of $x(Ni_{0.65}Zn_{0.35}Fe_2O_4)/(100-x)SiO_2$ nanocomposite powders by a modified sol–gel method. Mater. Chem. Phys. **113**, 342–348 (2009)
2. I. Chicinas, J. Optoelectron, Soft magnetic nanocrystalline powders produced by mechanical alloying routes. Adv. Mater. **8**, 439–448 (2006)
3. C. Suryanarayana, Mechanical alloying and milling. Prog. Mater Sci. **46**, 1–184 (2001)
4. A. Hajalilou, M. Hashim, R. Ebrahimi-Kahrizsangi, H. Mohamed Kamari, S. Kanagesan, Parametric optimization of $NiFe_2O_4$ nanoparticles synthesized by mechanical alloying. Mater. Sci. **32**, 281–291 (2014)
5. A. Hajalilou, M. Hashim, R. Ebrahimi-Kahrizsangi, H. Mohamed Kamari, N. Sarami, Synthesis and structural characterization of nano-sized nickel ferrite obtained by mechanochemical combustion. Ceram. Int. **40**, 5881–5887 (2014)
6. A. Azizi, S.K. Sadrnezhaad, Effects of annealing on phase evolution, microstructure and magnetic properties of mechanically synthesized nickel-ferrite. Ceram. Int. **36**, 2241–2245 (2010)
7. S. Bid, S.K. Pradhan, Characterization of crystalline structure of ball-milled nano-Ni–Zn-ferrite by Rietveld method. Mater. Chem. Phys. **84**, 291–301 (2004)
8. K. Kondo, T. Chiba, S. Yamada, Effect of microstructure on magnetic properties of Ni–Zn ferrites. J. Magn. Magn. Mater. **254–255**, 541–543 (2003)
9. D. Stoppels, Developments in soft magnetic power ferrites. J. Magn. Magn. Mater. **160**, 323–328 (1996)
10. V. Sepelak, D. Baabe, D. Mienert, D. Schultze, F. Krumeich, F.J. Litterst, K.D. Becker, Evolution of structure and magnetic properties with annealing temperature in nanoscale high energy-milled nickel ferrite. J. Magn. Magn. Mater. **257**, 377–386 (2003)
11. I.H. Gul, W. Ahmed, A. Maqsood, Electrical and magnetic characterization of nanocrystalline Ni–Zn ferrite synthesis by co-precipitation route. J. Magn. Magn. Mater. **320**, 270–275 (2008)
12. M. Srivastava, A.K. Ojha, S. Chaubey, A. Materny, Synthesis and optical characterization of nanocrystalline $NiFe_2O_4$ structures. J. Alloys Compd. **481**, 515–519 (2009)
13. M.R. Barati, S.A. Seyyed Ebrahimi, A. Badiei, The role of surfactant in synthesis of magnetic nanocrystalline powder of $NiFe_2O_4$ by sol–gel auto-combustion method. J. Non-Cryst. Solids **354**, 5184–5185 (2003)
14. J. Huo, M. Wei, Characterization and magnetic properties of nanocrystalline nickel ferrite synthesized by hydrothermal method. Mater. Lett. **63**, 1183–1184 (2009)
15. M. Ajmal, A. Maqsood, Influence of zinc substitution on structural and electrical properties of $Ni_{1-x}Zn_xFe_2O_4$ ferrites. Mater. Sci. Eng. B **139**, 164–170 (2007)
16. H.M. Yang, X.C. Zhang, W.Q. Ao, G.Z. Qiu, Formation of $NiFe_2O_4$ nanoparticles by mechanochemical reaction. Mater. Res. Bull. **39**, 833–837 (2004)
17. C.C. Hwang, C.S. Lin, G.P. Wang, C.H. Peng, S.L. Chung, A self-propagating high-temperature synthesis method for synthesis of zinc oxide powder. J. Alloys Compd. **467**, 514–523 (2009)
18. V. Sepelak, S. Wibmann, K.D. Becker, Magnetism of nanostructured mechanically activated and mechanosynthesized spinel ferrites. J. Magn. Magn. Mater. **203**, 135–137 (1999)
19. G.K. Williamson, W.H. Hall, X-ray line broadening from filed aluminium and wolfram. Acta Metall. **1**, 22–31 (1953)
20. A. Hajalilou, M. Hashim, M. Nahavandi, I. Ismail, Mechanochemical carboaluminothermic reduction of rutile to produce $TiC–Al_2O_3$ nanocomposite. Adv. Powder Technol. **25**, 423–429 (2014)
21. S. Mitra, S. Das, K. Mandal, S. Chaudhuri, Synthesis of a α-Fe_2O_3 nanocrystal in its different morphological attributes: growth mechanism, optical and magnetic properties. Nanotechnology **18**, 275608 (2007). doi:10.1088/0957-4484/18/27/275608
22. N. Lepot, M.K. Van Bael, H. Van den Rul, J. D'Haen, R. Peeters, D. Franco, J. Mullens, Synthesis of ZnO nanorods from aqueous solution. Mater. Lett. **61**, 2624–2627 (2007)
23. Y. Wang, J. Zhu, X. Yang, L. Lu, X. Wang, Preparation of NiO nanoparticles and their catalytic activity in the thermal decomposition of ammonium perchlorate. Thermochim. Acta **437**, 106–109 (2005)
24. B.D. Cullity, *Introduction to magnetic materials* (Addison-Wesley Publishing Co., Inc., Reading, MA, 1972)
25. S. Chikazumi, *Physics of magnetism* (Wiley, New York, 1959)
26. M. Georgea, A. Mary John, S.S. Naira, P.A. Joy, M.R. Anantharaman, Finite size effects on the structural and magnetic properties of sol–gel synthesized $NiFe_2O_4$ powders. J. Magn. Magn. Mater. **302**, 190–195 (2006)
27. M.A. Khadar, V. Biju, A. Inoue, Effect of finite size on the magnetization behavior of nanostructured nickel oxide. Mater. Res. Bull. **38**, 1341–1349 (2003)
28. W.J. Schuele, V.D. Deetscreek, Appearance of a weak ferromagnetism in fine particles of antiferromagnetic materials. J. Appl. Phys. **33**, 1136–1137 (1962)
29. J.M. Greneche, A. Ślawska-Waniewska, About the interfacial zone in nanocrystalline alloys. J. Magn. Magn. Mater. **215–216**, 264–267 (2000)
30. K.H.J. Buschow, F.R. de Boer, *Physics of magnetism and magnetic materials*, vol. 92 (Kluwer Academic/Plenum Publishers, New York, 2003)

31. V. Sepelak, I. Bergmann, A. Feldhoff, P. Heitjans, F. Krumeich, D. Menzel, F.J. Litterst, S.J. Campbell, K.D. Becker, Nanocrystalline nickel ferrite, NiFe2O4: mechanosynthesis, nonequilibrium cation distribution, canted spin arrangement, and magnetic behavior. J. Phys. Chem. C **111**, 5026–5033 (2007)

32. M. Gharagozlou, Study on the influence of annealing temperature and ferrite content on the structural and magnetic properties of $x(NiFe_2O_4)/(100 - x)SiO_2$ nanocomposites. J. Alloys Compd. **495**, 217–223 (2010)